

Skin-inspired scalable superhydrophobic coatings with strong mechano-chemical-thermal robustness

Hailong Zhang

Qilu University of Technology

Xinyu Bu

Qilu University of Technology <https://orcid.org/0000-0002-5640-1167>

wanbo li

City University of Hong Kong

Xingxiang Ji

Qilu University of Technology

Furong Tao

Qilu University of Technology

Ligang Gai

Qilu University of Technology

Haihui Jiang

Qilu University of Technology

Libin Liu

Qilu University of Technology

Zuankai Wang (✉ zuanwang@cityu.edu.hk)

City University of Hong Kong <https://orcid.org/0000-0002-3510-1122>

Article

Keywords:

Posted Date: January 25th, 2022

DOI: <https://doi.org/10.21203/rs.3.rs-1082414/v1>

License:   This work is licensed under a Creative Commons Attribution 4.0 International License.

[Read Full License](#)

Abstract

Designing environment-friendly, scalable superhydrophobic coatings with a wide spectrum of robustness in mechanochemical strength, interfacial adhesion, and flame retardancy is critical to low-carbon economy and green environment, especially for green buildings. Simultaneously achieving these preferred functionalities dominated by either interfacial or bulky properties has proved challenging. Herein, we propose an integral skin-inspired triple-layered coating (STC) that resolves conflicting demands imposed by individual features on the structure, component, and thermal property of materials. The STC demonstrates sustained anti-wetting and anti-corrosion even under harsh environments, strong adhesion and anti-abrasion, and excellent flame retardancy, all of which enhance its durability and lifetime so as to eliminate the maintenance and repair, thereby reducing cost and energy consumption. Together with facile spraying fabrication process, our STC paves the way to construct a green and resource-saving society.

Full Text

Improving energy utilization and reducing energy loss are conducive to developing a green and healthy society. As the protective barrier and mediator interacting with external environments, surfaces with self-cleaning, chemical inertness and long durability are highly demanded to achieve optimal energy efficiency. For example, the energy consumption from buildings alone exceeds 10% of the total energy consumption¹ and thus, controlling the structural, chemical and thermal properties of building surfaces to impart multifunctions in complex operating environments including varying temperature and humidity is critical. Of special interest is natural superhydrophobic surfaces found on the skins of many living organisms²⁻⁵, and bio-inspired artificial coatings widely adopted in energy-related processes such as self-cleaning⁶⁻⁸, thermal management⁹⁻¹¹, energy harvesting¹²⁻¹⁴, anti-fogging^{15,16}, anti-biofouling¹⁷, and anti-icing^{18,19}. In spite of extensive progress, practical implementations of superhydrophobic coatings with preferred functionalities and durability for energy saving dictate a wide-spectrum robustness including mechanochemical strength, high adhesion with substrates, and flame resistance, a challenge remaining unsolved to date.

However, it appears difficult to mutually achieve all these features in one design. First, from the structure perspective, achieving ideal superhydrophobicity generally requires the design of micro/nanostructures, which, on the other hand, are susceptible to external dynamic mechanical load (e.g., crush and abrasion) owing to mechanical stress concentration^{20,21}. Second, to obtain a high adhesion with underlying substrates, the coating should be equipped with sufficient polar building blocks, while increasing the polarity inevitably compromises surface hydrophobicity²². Third, in high temperature and dry environments, satisfying flame retardancy and superhydrophobicity is also elusive owing to a simple fact that most of organic flame retardants are polar. To date, most superhydrophobic coatings with additional functions are usually designed separately, and also fabricated using complicated processes, for example, top-down and multi-step etching and molding, which pose severe limits to mass

production and real-world applications^{23,24}. Taken together, developing a co-design strategy that simultaneously achieves the integral functionalities by decoupling distinctive requirements on the structure, component, thermal property of coatings is still challenging.

Our design is inspired by human skin (Fig. 1a), featuring with a hierarchical structure made of three layers including epidermis, dermis, and subcutaneous tissue, respectively. The epidermis layer is the outermost layer of the skin, serving as a protective barrier over the body's surface. The middle layer, dermis, is mostly composed of collagen and elastin, in which collagen fibers and elastic fibers are intertwined and buried in the matrix to strengthen and support the skin. And the subcutaneous tissue consists of loose connective tissue and adipose tissue, which intimately link skin and muscles.

Fig. 1b shows the schematic drawing of the skin-inspired triple-layered coating (STC) that exhibits collective performances by taking advantage of three levels of gradient in roughness/wetting, strength and flame retardancy along its triple layers. A common component within STC is polar epoxy resin matrix which can be chemically functionalized, physically mixed with fillers, and molecularly modified to give rise to desired functionalities. Specifically, the epidermis-mimicking top layer with superhydrophobicity and anti-abrasion is constructed by the choice of fluorinated epoxy resin (Supplementary Fig. 1) with regularly dispersed fluorinated cellulose/SiO₂ particles (Supplementary Fig. 2). In the dermis-like middle layer, the amount of fluorinated cellulose and SiO₂ in the fluorinated epoxy resin is 50% reduced to act as a bridge between the top layer and bottom layer. To endow strong bonding with various substrates, we choose the utility of un-fluorinated epoxy resin in the bottom layer, followed by molecular mixing with 9,10-dihydro-9-oxa-10-phosphaphenanthrene-10-oxide (DOPO) to give rise to enhanced flame retardancy (Fig. 1b). One key innovation in our design lies in decoupling the distinctive requirements imposed by anti-wetting, anti-abrasion and anti-flaming into three layers while preserving a continuous interface across the triple-layer. To ensure optimal performances in each layer and the entire STC coating, we first compared its superhydrophobicity and anti-abrasion properties by tuning the mass fraction of epoxy matrix across triple-layer, the mass fraction of fillers (fluorinated cellulose and SiO₂) in epoxy in the top layers (Supplementary Fig. 3).

The STC with the optimized components is fabricated by a three-stage spraying/curing process, in which the temperature and the duration of each curing stage are carefully tailored to allow for conformal adhesion with underlying substrate and bonding within layers. In particular, the bottom layer was sprayed and cured at room temperature, a process distinct from existing in standard spraying coating. To impart an integral adhesion within layers, a soft-curing at a temperature of 45 °C for a duration of 30 mins was introduced after spraying the middle layer, followed by spraying the top layer with a complete curing (120 °C and 10 h). To demonstrate the superior properties of STC, a monolayer coating (Control 1) and a bilayer coating (Control 2), both of which have the same compositions as STC, were also fabricated by using similar preparation process (Supplementary Fig. 4).

Fig. 1c shows a representative STC sample fabricated on Al substrate with a size up to 20 inches. Its surface exhibits a water-repellant property with a water contact angle ~172.3°. This high contact angle is

rendered by the presence of hierarchically micro/nanostructures as well as the low surface energy of fluorine element, as evidenced by scanning electron microscopic (SEM) measurement and XPS measurement (Fig. 1d and inset). The micro-sized celluloses in both the surface and bulk of STC can be reflected by confocal fluorescence microscope measurement, which shows the formation of the 3D intertwined framework labelled in green (Fig. 1e, Supplementary Fig. 5 and 6). As shown in the cross-sectional electron microprobe (EM) image of the fabricated STC (Fig. 1f), the boundary between each layer of STC can be clearly discerned. In particular, the bottom layer of STC shows the presence of a variety of polar groups (Supplementary Fig. 7), which is in striking contrast to that of Control 1 and Control 2 (Supplementary Fig. 8 and 9). On the basis of the EM mapping as shown in Fig. 1g and 1h, both silicon and fluorine contents in the top layer are higher than those in the middle layer, and there is no apparent existence of fluorine element in the bottom layer. Moreover, phosphorus element resulting from DOPO is found to be distributed in the bottom layer alone, as shown in Fig. 1i and XPS measurement (Supplementary Fig. 10).

Practical applications of coatings, particularly in green buildings, involve various operating environments. At high humidity and high temperature, conventional superhydrophobic coatings are easy to collapse owing to the penetration of tiny water droplets into rough structures. When the STC was exposed to hot steam ($\sim 100\text{ }^{\circ}\text{C}$) using home-made hot steam device (Supplementary Fig. 11), it still maintained a sustained anti-wetting property. As shown in Fig. 2a, high-temperature water vapor first condensed into discrete small droplets with an average size of $400\text{ }\mu\text{m}$, and then easily rolled off the surface by gravity or coalescence-induced jumping (Supplementary Movie 1), otherwise impossible to be achieved for control samples (Supplementary Fig. 12). In the opposite condition, we put the STC into a refrigeration cycle machine with a programmable temperature ranging from $0\text{ }^{\circ}\text{C}$ to $-70\text{ }^{\circ}\text{C}$ and examined the ice formation by depositing deionized water (2 mL) on its surface at different locations with $10\text{ }^{\circ}\text{C}$ intervals. We found that the weight of ice on STC-Al sheet is only about 1 g at $-30\text{ }^{\circ}\text{C}$, which is 6-fold smaller than that on the pristine Al sheet. Even at $-70\text{ }^{\circ}\text{C}$, the weight of the ice on STC-Al sheet is about 58.4% of that on pristine Al sheet, indicating that the STC-Al sheet has excellent anti-icing effect (Fig. 2b, Supplementary Fig. 13). In addition, by applying a small external force on the STC-Al sheet, the ice fell off as a whole piece easily owing to the presence of air barrier layer²⁵, whereas the ice on pristine Al sheet was difficult to be removed, indicating an extremely low adhesion of STC surface (Fig. 2c, Supplementary Fig. 14 and Movie 2).

In addition to maintaining a stable anti-wetting property, the presence of air barrier layer in STC also reduces its contact area with the corrosive medium and thus promotes anti-corrosion and durability²⁶⁻²⁹. Here, we combined the copper-accelerated acetic acid salt spray test and electrochemical measurement to assess the corrosion resistance of the coating (Supplementary Fig. 15). The STC-Al sheet yields the biggest E_{corr} (-0.01 V) and the smallest I_{corr} ($2.337 \times 10^{-4}\text{ A}\cdot\text{cm}^{-2}$) compared with other samples (Fig. 2d), showing a strong corrosion resistance. In the Nyquist spectrum (Fig. 2e), the impedance value significantly increases from $2.7\text{ }\Omega\cdot\text{cm}^{-2}$ for pristine Al sheet to $590.1\text{ }\Omega\cdot\text{cm}^{-2}$ for STC-Al sheet, indicating that the STC can significantly protect Al metal from corrosion. The mass loss rate per unit area (ΔK_{MLR} ,

see notes in Supplementary Information) was used to assess the corrosion resistance of the coating. As shown in Supplementary Fig. 16, after 120 h corrosion, the surface morphology of STC rarely changes whereas noticeable corrosion pits occur to control samples. The ΔK_{MLR} of the STC-Al sheet decreases to below $1 \text{ g}\cdot\text{m}^{-2} \text{ h}^{-1}$, which is much lower than that of Control 1-Al sheet ($14.8 \text{ g}\cdot\text{m}^{-2} \text{ h}^{-1}$), Control 2-Al sheet ($8.6 \text{ g}\cdot\text{m}^{-2} \text{ h}^{-1}$) and the pristine sample ($22 \text{ g}\cdot\text{m}^{-2} \text{ h}^{-1}$) (Fig. 2f). Even after 300 h, the STC-Al sheet was slightly corroded while control samples are completely destroyed (Fig. 2g-j, Supplementary Movie 3). In addition, the STC still maintains robust superhydrophobicity and high corrosion resistance in corrosive environments such as after immersing in aqua regia for 40 h and in 12 M NaOH solution for 60 min (Supplementary Fig. 17 and 18). These results demonstrate the durable anti-wetting properties in various extreme conditions.

One limitation in conventional coatings lies in the difficulty in solving the tradeoff between anti-wetting and anti-abrasion owing to the mechanical fragility and easy damage of micro/nanoscale roughness. The abrasion resistance of our sample was tested using the Taber abrasion tester (Supplementary Fig. 19). Even after 3,000 cycles under a 250 g load, the θ_C is larger than $\sim 150^\circ$ and θ_R is less than 10° , a performance at least 10 times higher than our previous work³⁰ and other existing studies³¹⁻³⁴ (Fig. 3a-c, Supplementary Movie 4). Moreover, even under a 750 g load, our sample performed well up to ~ 1000 cycles, suggesting simultaneously preserving the anti-wetting and anti-abrasion property. In contrast, without the use of the layered-design, the superhydrophobic properties of Control 1 and Control 2 were collapsed after 300 and 1000 cycles' testing, respectively (Fig. 3a, 3b, Supplementary Movie 5 and 6). More importantly, the STC is also tolerant to various sharp objects (Supplementary Movie 7) such as steel-wool (width: $0.13\pm 0.05 \text{ mm}$), screwdriver, steel-blade (feather-cut special: $58*13.35*0.15 \text{ mm}$), utility knife (blade angle: 30°) and hammer attack. This is different from the armor design reported by us before³⁰ where the microscale cavity is filled with mechanically weak resin which can be easily damaged by sharp tips. Thus, our STC manifests both anti-wettability and mechanical stability, a property extending from the surface to the middle layer. Without the optimal control of components fraction in triple-layer, i.e., mainly the mass ratio of fillers in the top and middle layer, the STC samples are susceptible to sharp variation in structural integrity, and hence their mechanical robustness and anti-wetting performances are compromised as opposed to their counterparts (Fig. 3d), demonstrating the essence of preserving gradually-varying and continuous interfaces across the triple-layer.

We also conducted adhesion test using the American Society of Testing Materials (ASTM) D3359 standard (Supplementary Fig. 20) to examine the bonding capability of the as-fabricated STC with underlying glass substrate. Briefly, we used multiple tap cutters to create regular grids with an interval of 1 mm on the STC surface. Then the coating is compressed by 3 M tape under a uniform load of 2 kg, followed by peeling off (Fig. 3e). We found that the coating is free of any apparent detachment of fragments and maintains a superior structural integrity, exhibiting a performance that meets the ASTM 5B standard (Fig. 3f). In contrast, without the layered-design, control samples suffer from limited adhesion strength as evidenced by the easy peeling of coating from glass substrate (Fig. 3g and 3h). Such a strong adhesion can still be maintained even when the STC was brought to harsh treatment. As

shown in Supplementary Fig. 21, after cutting and immersing in water at room temperature for 24 hours or in boiling water for 20 minutes and in aqua regia for 40 hours, there is no pronounced change in the adhesion property of the STC after being peeling-off using 3 M tape.

In addition to preserving an enhanced mechano-chemical robustness, our STC coating also demonstrates anti-flaming capacity so as to extend its lifetime and avoid unnecessary repair, a property essential for safety at extremely high temperatures and dry conditions. We applied our coating to different models such as wooden house of different sizes and electric circuits. First, for a STC-coated model with a size of 15.6 cm×18.6 cm×23.3 cm, it was partially burned when being ignited using an alcohol blowtorch for 110 s, however, it spontaneously self-extinguished at 135 s (Fig. 4a, Supplementary Movie 8). In contrast, the pristine wooden house model was ignited within 45 s and went into fire within 180 s, reaching a flame temperature up to 726.5 °C as evidenced by thermal infrared camera measurement. When a large STC-coated wooden house with 1.2 m×1.2 m×1.4 m was brought to a jet gun with an outer flame temperature of 1300 °C for 30 mins, there was no igniting observed. As a comparison, without the application of STC, the pristine wooden house with the same size gradually became a pile of ash within 25 mins (Supplementary Movie 9). Similar trend was also found when spraying STC as a protective coating on supercapacitors in electrical circuits. As shown in Supplementary Fig. 22, the STC-coated supercapacitor can still light up LED even under 10 s of ignition, while the pristine supercapacitor is burned within 3 s (Supplementary Movie 10). All these experiments indicate that our coating has good flame retardancy and manifests its practical value after large-scale spraying process. Notable, these enhanced flame retardancy is achieved with only 2 wt% DOPO loading, a fraction low enough without sacrificing the mechanical property of the material³⁵⁻³⁷.

We then sprayed STC and control samples on polyurethane (PU) to quantitatively characterize the flame retardancy of STC using a cone calorimeter. First, the limiting oxygen index of STC-PU in our experiment is ~ 26.7 %, which is higher than a critical flammable value of 22% in air and also higher than that of Control 1-PU (24.7 %) and Control 2-PU (24.2 %) (Fig. 4b). Second, the time to ignition of STC-PU is also 75% longer than that of pristine PU (Fig. 4b). Third, the maximum heat release rate of STC-PU is about 79.6 kW·m⁻², which is 48.2 % of Control 2-PU and 33.4 % of Control 1-PU as well as 19.9 % of pristine PU, indicating that STC can effectively suppress heat release (Fig. 4c). Similarly, the total heat release of STC-PU is only one third of that of pristine-PU (Fig. 4d). The release of toxic gas (CO₂, CO), specific extinction area, effective heat of combustion and mass loss rate were also measured to prove the flame retardancy of STC (Supplementary Fig. 23). The enhanced antflaming robustness of STC directly results from the flame retardant imbedded in the bottom layer. Upon in contact with fire, DOPO can generate orthophosphoric acid and release P containing free radicals (e.g. PO•), which can capture free radicals of H• and HO• to terminate combustion reaction. The orthophosphoric acid also burns into a coke layer to cut off oxygen, further hampering the combustion reaction (Supplementary Fig. 24 and 25). Second, we also considered the effect of air barrier layer trapped in hierarchically micro/nanostructures due to the low thermal conductivity of air (~0.026 W/(m·K)). To do so, we deposited STC, Control 1 and Control 2 on steel substrates, respectively, all of which were then brought into heating using alcohol blowtorch

(Supplementary Fig. 26). The measured surface temperature of STC is 306 °C, which is 21.4% and 26.2% smaller than those of Control 1 (389.4 °C) and Control 2 (414.7 °C), suggesting the suppression of heat transfer owing to the presence of air layer (Fig. 4e-g).

In conclusion, we demonstrate a skin-inspired, triple-layered multifunctional superhydrophobic coating exhibiting superior mechanical-chemical-thermal properties to existing coatings (Supplementary Fig. 27). Combining these desirous performances with the facile solution-processible fabrication process, the co-design strategy provides a new approach for engineering robust coatings that expand the application domains from green buildings to other scenarios such as vehicles, airplane wings, marine vessels, oil pipelines, and power lines.

Declarations

Acknowledgements

We acknowledge the support from the Introduction and Cultivation Plan of Young Innovative Talents in Colleges and Universities of Shandong Province, Key Project of Shandong Natural Science Foundation (ZR2020KE005), Research Grants Council of Hong Kong (No. C1006-20WF, No. 11213320), Tencent Foundation through the XPLOER PRIZE, Innovation and Technology Council (No. 9440248).

Author contributions

H. Z., X. B., L. L. and Z. W. conceived the research. L. L. and Z. W. supervised the research. H. Z. and X. B. carried out the experiment. W. L. and X. J. collected and analyzed the data. F. T., L. G. and H. J. prepared the experimental apparatus. All authors contributed to the interpretation and drafting of the paper.

Competing interests

The authors declare no competing interests.

Additional information

Supplementary information is available for this paper at <https://www.nature.com/reprints>:

Reprints and permissions information is available at www.nature.com/reprints.

Correspondence and requests for materials should be addressed to L.L. or Z.W.

Publisher's note: Springer Nature remains neutral with regard to jurisdictional claims in published maps and institutional affiliations.

References

1. Wicklein, B. et al. Thermally insulating and fire-retardant lightweight anisotropic foams based on nanocellulose and graphene oxide. *Nat. Nanotechnol.* **10**, 277–283 (2015).
2. Rauner, N. et al. A Coating that combines lotus-effect and contact-active antimicrobial properties on silicone. *Adv. Funct. Mater.* **28**, 1801248 (2018).
3. Eder, M. Amini, S. & Fratzl, P. Biological composites—complex structures for functional diversity. *Science* **362**, 543–547 (2018).
4. Liu, M. Wang, S. & Jiang, L. Nature-inspired superwettability systems. *Nat. Rev. Mater.* **2**, 17036 (2017).
5. Wakerley, D. et al. Bio-inspired hydrophobicity promotes CO₂ reduction on a Cu surface. *Nat. Mater.* **18**, 1222–1227 (2019).
6. Deng, X. Mammen, L. Butt, H. J. & Vollmer, D. Candle soot as a template for a transparent robust superamphiphobic coating. *Science* **335**, 67–70 (2012).
7. Lu, Y. et al. Robust self-cleaning surfaces that function when exposed to either air or oil. *Science* **347**, 1132–1135 (2015).
8. Geyer, F. et al. When and how self-cleaning of superhydrophobic surfaces works. *Sci. Adv.* **6**, eaaw9727 (2020).
9. Lo, C. W. Chu, Y. C. Yen, M. H. & Lu, M. C. Enhancing condensation heat transfer on three-dimensional hybrid surfaces. *Joule* **3**, 2806–2823 (2019).
10. Li, W. et al. Supercapillary architecture-activated two-phase boundary layer structures for highly stable and efficient flow boiling heat transfer. *Adv. Mater.* **32**, 1905117 (2020).
11. Ma, Z. et al. Bioinspired, highly adhesive, nanostructured polymeric coatings for superhydrophobic fire-extinguishing thermal insulation foam. *ACS Nano* **15**, 11667–11680 (2021).
12. Xu, W. et al. A droplet-based electricity generator with high instantaneous power density. *Nature* **578**, 392–396 (2020).
13. Xu, W. & Wang, Z. Fusion of slippery interfaces and transistor-inspired architecture for water kinetic energy harvesting. *Joule* **4**, 2527–2531 (2020).
14. Feng, S. et al. Three-dimensional capillary ratchet-induced liquid directional steering. *Science* **373**, 1344–1348 (2021).
15. Mouterde, T. et al. Antifogging abilities of model nanotextures. *Nat. Mater.* **16**, 658–663 (2017).
16. Yoon, J. et al. Wet-style superhydrophobic antifogging coatings for optical sensors. *Adv. Mater.* **32**, 2002710 (2020).
17. Liu, J. et al. Elastic superhydrophobic and photocatalytic active films used as blood repellent dressing. *Adv. Mater.* **32**, 1908008 (2020).
18. Jung, S. Tiwari, M. K. Doan, N. V. & Poulikakos, D. Mechanism of supercooled droplet freezing on surfaces. *Nat. Commun.* **3**, 615 (2012).

19. Wang, L. Gong, Q. Zhan, S. Jiang, L. & Zheng, Y. Robust anti-icing performance of a flexible superhydrophobic surface. *Adv. Mater.* **28**, 7729–7735 (2016).
20. Tian, X. Verho, T. Ras, R. H. A. Moving superhydrophobic surfaces toward real-world applications. *Science* **352**, 142 (2016).
21. Zhang, W. Wang, D. Sun, Z. Song, J. & Deng, X. Robust superhydrophobicity: mechanisms and strategies. *Chem. Soc. Rev.* **50**, 4031 (2021).
22. Zhu, P. Kong, T. Tang, X. & Wang, L. Well-defined porous membranes for robust omniphobic surfaces via microfluidic emulsion templating. *Nat. Commun.* **8**, 15823 (2017).
23. Zhang, H. et al. Versatile, mechanochemically robust, sprayed superomniphobic coating enabling low surface tension and high viscous organic liquid bouncing. *Chem. Eng. J.* **402**, 126160 (2020).
24. Li, Y. Chen, S. Wu, M. & Sun, J. All spraying processes for the fabrication of robust, self-healing, superhydrophobic coatings. *Adv. Mater.* **26**, 3344–3348 (2014).
25. Dhyani, A. et al. Design and applications of surfaces that control the accretion of matter. *Science* **373**, eaba5010 (2021).
26. Zang, D. et al. Corrosion-resistant superhydrophobic coatings on Mg alloy surfaces inspired by lotus seedpod. *Adv. Funct. Mater.* **27**, 1605446 (2017).
27. Gomaa, H. Tembely, M. Esmail, N. & Dolatabadi, A. Bouncing of cloud-sized microdroplets on superhydrophobic surfaces. *Physics of Fluids* **32**, 122118 (2020).
28. Wei, J. et al. Efficient protection of Mg alloy enabled by combination of a conventional anti-corrosion coating and a superamphiphobic coating. *Chem. Eng. J.* **390**, 124562 (2020).
29. Chen, X. & Selloni, A. Introduction: Titanium dioxide (TiO₂) nanomaterials. *Chem. Rev.* **114**, 9281–9282 (2014).
30. Wang, D. et al. Design of robust superhydrophobic surfaces. *Nature* **582**, 55–59 (2020).
31. Qing, Y. Shi, S. Lv, C. & Zheng, Q. Microskeleton-nanofiller composite with mechanical super-robust superhydrophobicity against abrasion and impact. *Adv. Funct. Mater.* **30**, 1910665 (2020).
32. Peng, C. Chen, Z. & Tiwari, M. K. All-organic superhydrophobic coatings with mechanochemical robustness and liquid impalement resistance. *Nat. Mater.* **17**, 355–360 (2018).
33. Gao, J. Martin, A. Yatvin, J. White, E. & Locklin, J. Permanently grafted icephobic nanocomposites with high abrasion resistance. *J. Mater. Chem. A* **4**, 11719–11728 (2016).
34. Wu, B. et al. Inverse infusion processed hierarchical structure towards superhydrophobic coatings with ultrahigh mechanical robustness. *Chem. Eng. J.* **387**, 124066 (2020).
35. Duan, H. Chen, Y. Ji, S. Hu, R. & Ma, H. A novel phosphorus/nitrogen-containing polycarboxylic acid endowing epoxy resin with excellent flame retardance and mechanical properties. *Chem. Eng. J.* **375**, 121916 (2019).
36. Chen, R. et al. Synthesis of chitosan-based flame retardant and its fire resistance in epoxy resin. *Carbohydr. Polym.* **245**, 116530 (2020).

37. Yusuf, A. Avvaru, V. S. Dirican, M. Sun, C. & Wang, D. Y. Low heat yielding electrospun phosphenanthrene oxide loaded polyacrylonitrile composite separators for safer high energy density lithium-ion batteries. *Appl. Mater. Today* **20**, 100675 (2020).

Figures

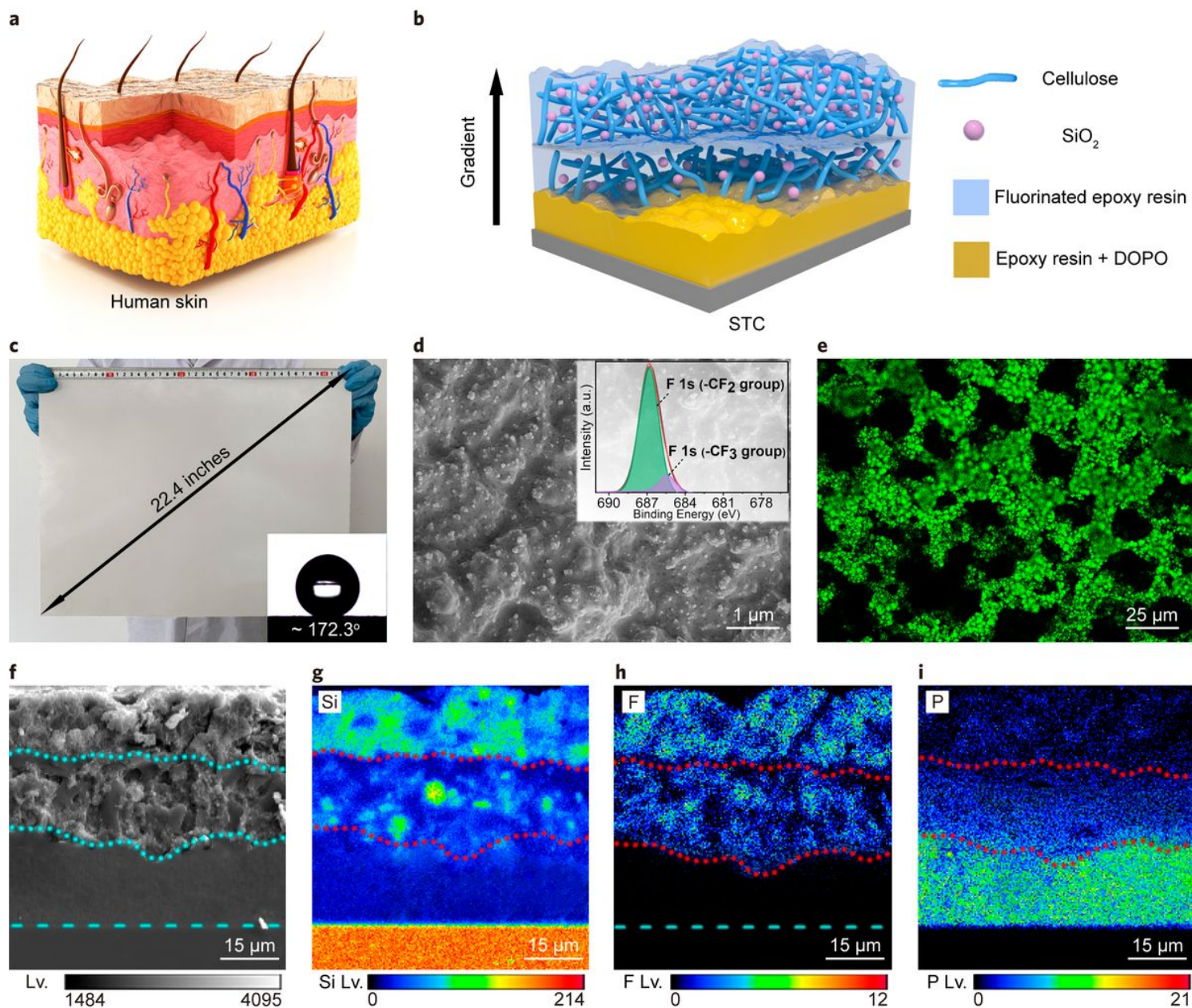


Figure 1

STC Design and characterization. **a**, Schematic diagram of human skin. **b**, Schematic diagram of STC. The bottom layer is composed of epoxy resin and DOPO, providing adhesion strength and flame retardancy. The middle and top layers are composed of fluorinated epoxy resin, cellulose and SiO₂. The middle layer consists of a smaller amount of cellulose and SiO₂ and a larger amount of fluorinated epoxy

resin than that in the top layer, which provides a wetting/strength gradient bridge between the top layer and bottom layer, allowing the coating to remain adhesiveness and hydrophobicity as a whole if the top layer is irreversibly damaged. **c**, The photograph of the sprayed STC on a 45 cm x 30 cm Al sheet with water contact angle about 172.3° (insets). **d**, The SEM image and the XPS spectra (insets) of STC surface. **e**, 3D map of confocal microscopy of fluorescently labeled cellulose. **f**, The electron microprobe (EM) image of cross-sectional STC. The layering boundary is marked by a blue dotted line in the EM images. **g-i**, Elemental mapping of the EM image of the cross-sectional STC. Differences in elemental distribution content indicate the triple-layered structure of STC. The layering boundary is marked by a red dotted line in mapping images.

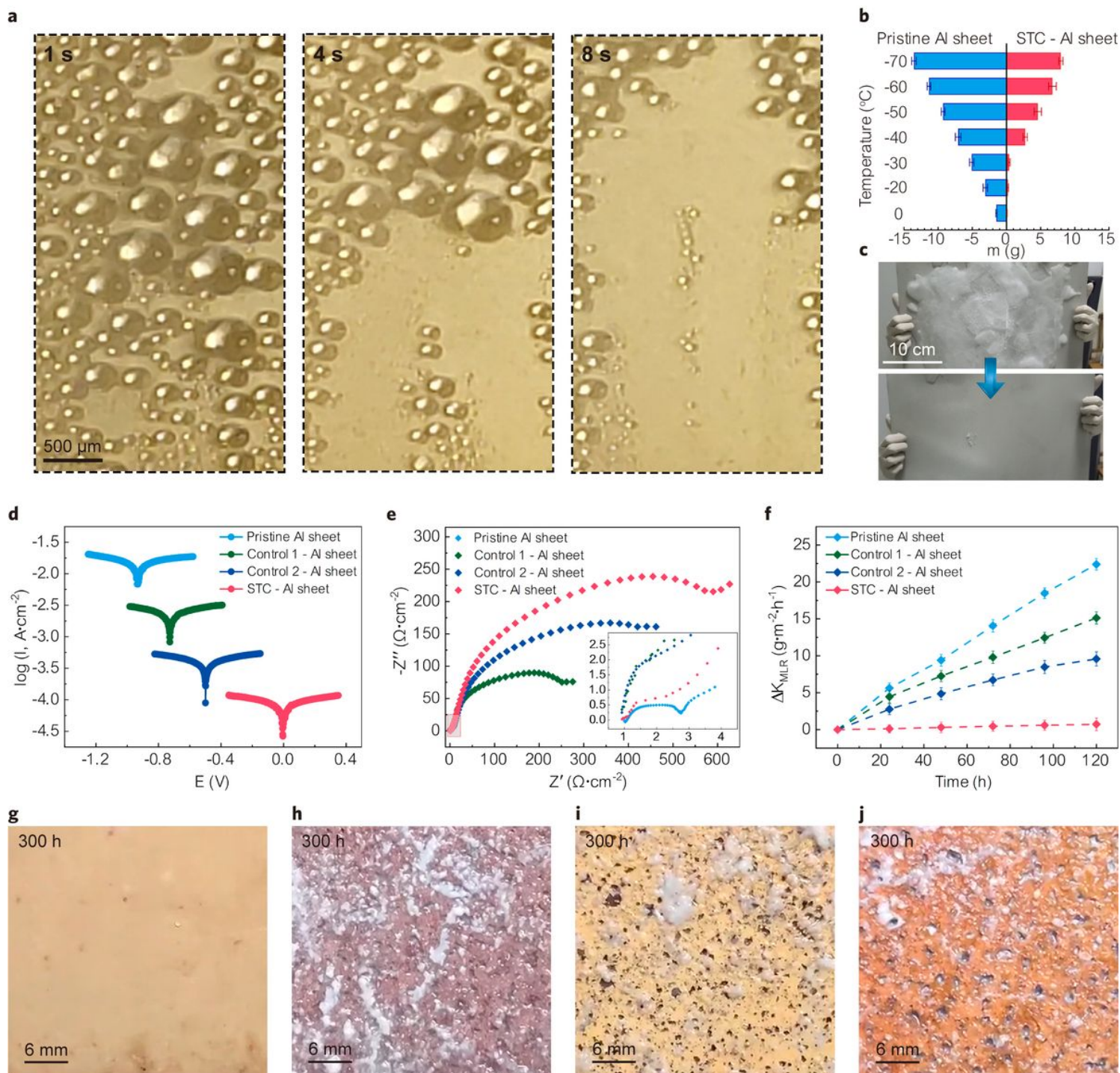
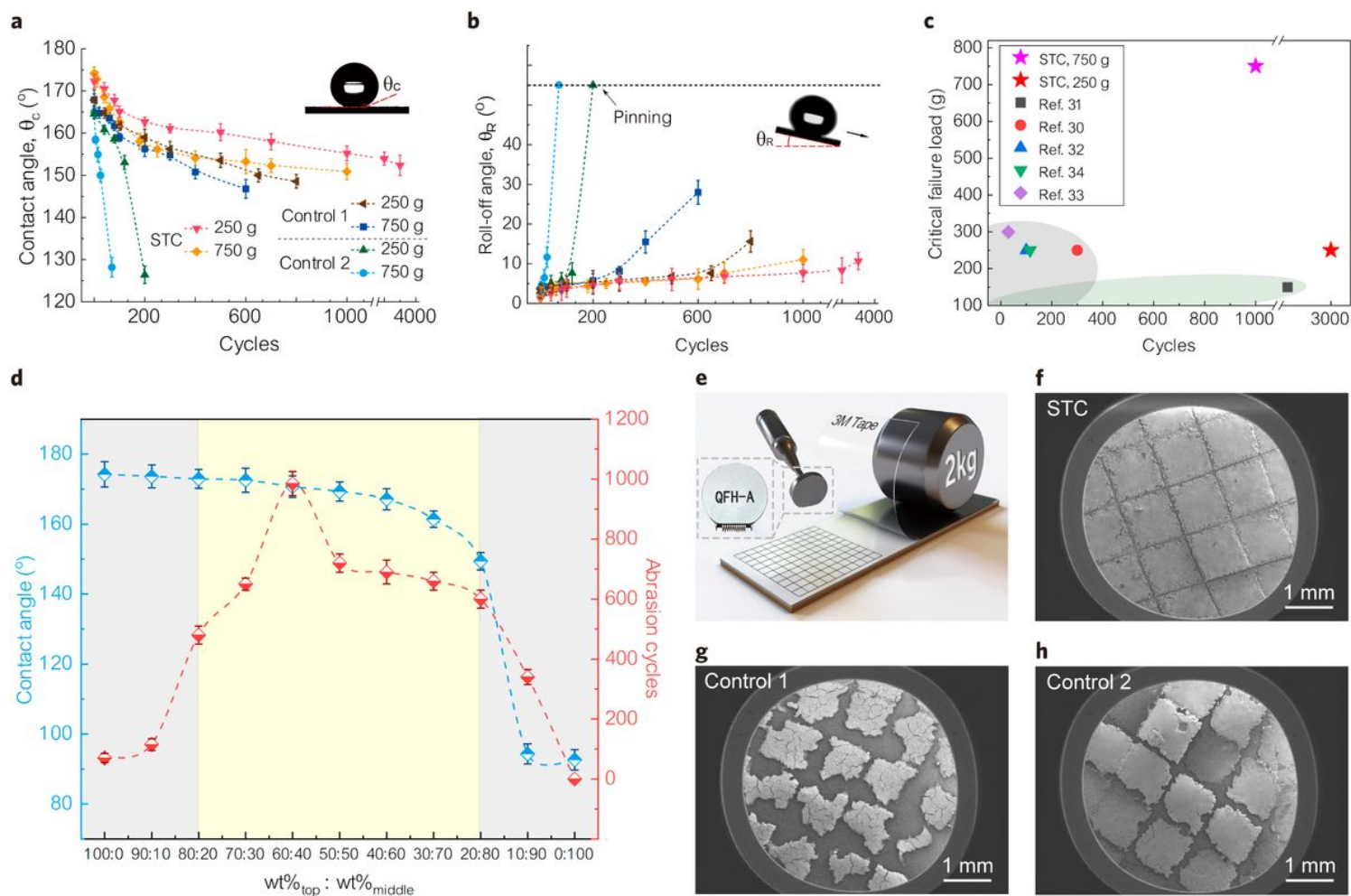


Figure 2

Anti-wetting and chemical robustness. **a**, Photograph of hot stream condensation on STC-Al surface. **b**, Anti-icing experiment of pristine Al sheet and STC-Al sheet. **c**, Photograph of deicing experiment on STC-Al sheet. **d**, Comparison of corrosion potential and corrosion current of different samples. **e**, Electrochemical impedance spectroscopy diagram of different test samples. **f**, The change of the mass loss rate per unit area (ΔK_{MLR} , $\Delta K_{MLR} = (m_t - m_0) / (TS)$, where m_t corresponds to the mass of sample under different test times, m_0 is the initial mass of the sample, T represents the test time, and S represents the area of the sample) of different test samples over time. ΔK_{MLR} of STC-Al sheet is at a lowest level during the whole test. Photographs of corrosion degree of **(g)** STC-Al sheet, **(h)** pristine Al sheet, **(i)** Control 1-Al sheet and **(j)** Control 2-Al sheet, after copper-accelerated acetic acid salt spray test for 300 h, respectively.

**Figure 3**

Mechanical robustness. The changes in **(a)** water contact angle (θ_c) and **(b)** water roll-off angle (θ_R) of STC, Control 1 and Control 2 with Taber abrasion cycles under two different loads (250 g and 750 g). For STC, after 3,000 cycles abrasion under a 250 g load and 1,000 cycles under a 750 g load, θ_c is $\sim 150^\circ$ and θ_R is less than 10° , respectively. **c**, Comparison of the antiabrasion performance of STC with existing superhydrophobic surfaces. All the references use Taber abrasion test method. **d**, The effect of gradient

mass ratio of fillers in top and middle layers on the superhydrophobicity and mechanical robustness. **e**, A schematic of adhesion test. **f-h**, SEM images of STC, Control 1 and Control 2 after adhesion test, respectively. After peeling off, the retention of STC is significantly better than that of Control 1 and Control 2.

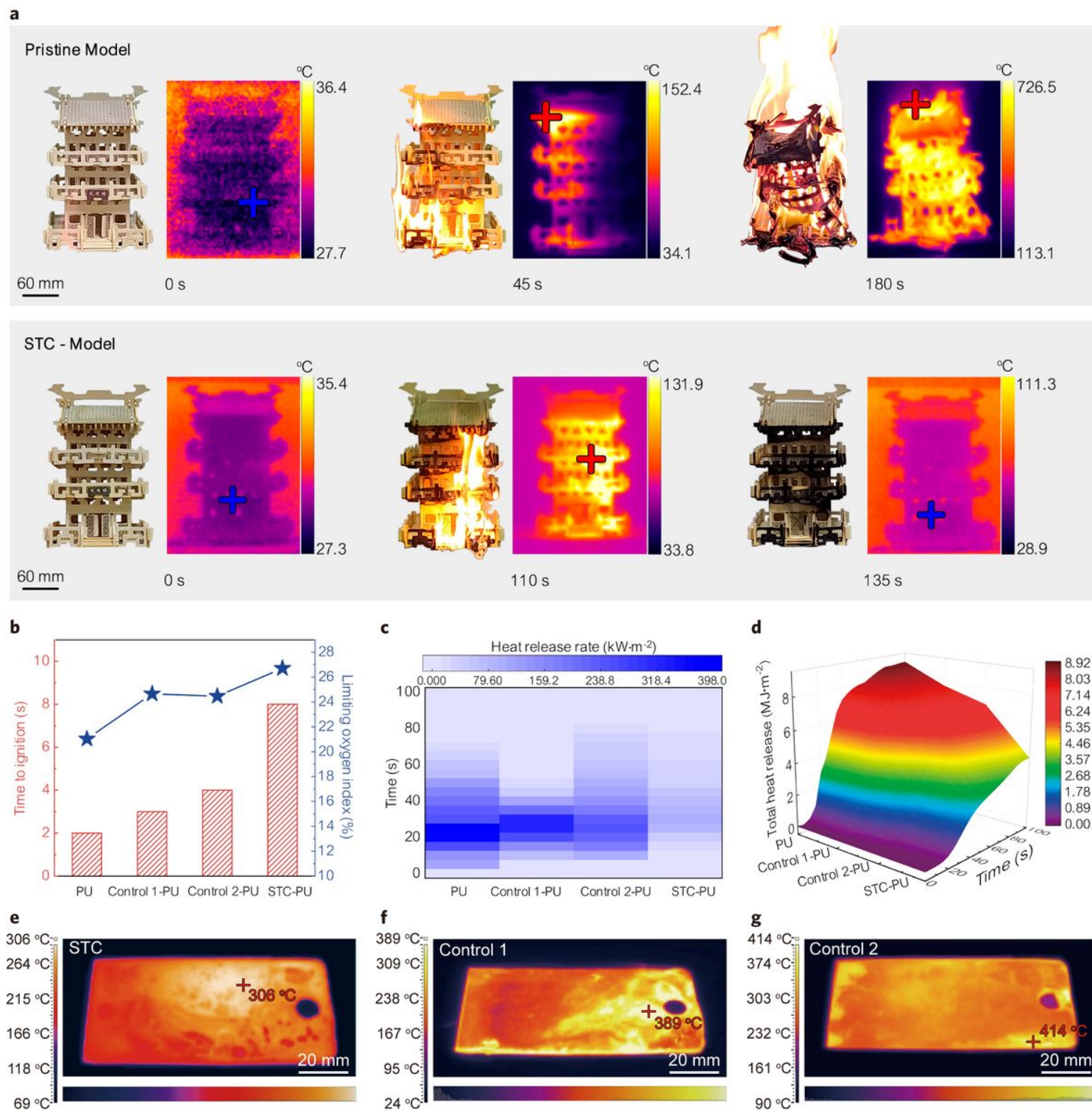


Figure 4

Antiflaming robustness. a, Photograph of the changes in combustion state over time. The pristine wooden house model was ignited after continuously igniting for 45 s. STC-model was partially ignited after 110 s and then self-extinguished at 135 s. **b,** Diagram of time to ignition and limiting oxygen index of pristine PU, Control 1-PU, Control 2-PU and STC-PU. **c,** Diagram of heat release rate of different samples. The maximum heat release rate of the STC-PU is about four times lower than that of pristine PU. **d,** Total heat release diagram of coated PU and pristine PU samples. **e-g,** Thermal infrared image of STC coated-steel and control sample coated-steel after heating by alcohol blowtorch.

Supplementary Files

This is a list of supplementary files associated with this preprint. Click to download.

- [MovieS1.mp4](#)
- [NatMatcoatingSupplementarymaterialsfinal.docx](#)
- [MovieS5Control1.mp4](#)
- [MovieS6Control2.mp4](#)
- [MovieS8.mp4](#)
- [MovieS10.mp4](#)
- [MovieS2.mp4](#)
- [MovieS3.mp4](#)
- [MovieS9.mp4](#)
- [MovieS7.mp4](#)
- [MovieS4.mp4](#)